

Spark Plasma Sintering and Upsetting of a Gas-Atomized/ Air-Atomized Al Alloy Powder Mixture

Mehmet Masum Tünçay, José Alberto Muñiz-Lerma, Donald Paul Bishop, and Mathieu Brochu

(Submitted May 25, 2017; in revised form August 10, 2017; published online September 21, 2017)

Al-Zn-Mg-Cu alloy powder, Alumix 431D, was modified by replacing the native air-atomized pure Al particles with gas-atomized pure Al. Samples were sintered using spark plasma sintering (SPS), and upset forging was applied to the sintered samples by SPS. Densities over 98 and 99% of theoretical were obtained for the sintered and forged samples, respectively. Microstructural analysis and characterization of all samples were done using energy-dispersive spectroscopy and x-ray diffraction. Mechanical properties were evaluated using microhardness and flexural strength and strain measurements. The microhardness value of the T6 tempered sample was comparable to that of its wrought counterpart AA7075. Particle bonding after sintering was incomplete and reveals that composite oxide layer of Al-Zn-Mg-Cu alloy powder is difficult to disrupt, and it is necessary to apply a secondary process like forging to improve particle bonding. The loss in ductility following T6 tempering is ascribed to void formation due to the dissolution of the secondary phases, remaining undissolved precipitates, and a localized lack of cohesion between particles.

Keywords Al alloys, forging, mechanical properties, powder blend, spark plasma sintering

1. Introduction

The native oxide film present on the surface of powder particles is a technical challenge inherent to powder metallurgy (P/M) processing of Al alloys. This tenacious oxide layer is thermodynamically stable and prevents sintering when metal-to-metal contact is not provided through disruption of the oxide layer (Ref 1, 2). Successful sintering of high-strength Al alloys, such as Alumix 431D alloy (P/M version of AA7075), which is a powder blend of air-atomized Al particles and master alloy particles containing Al, Zn, Mg, and Cu (Ref 3), can be obtained by liquid-phase sintering (Ref 4). This sintering approach disrupts the stable oxide layer covering the Al particles. Nevertheless, heterogeneous shrinkage of the powder compact during liquid-phase sintering is a drawback in terms of near-net-shape processing (Ref 4). As an alternative, forging of Al P/M products can be used to close the residual porosity and disrupt the oxide film around the powder particles through the application of high strains and strain rates (Ref 5). Upsetting is a type of forging in which a workpiece is placed under pressure between two parallel plates to reduce initial height without extensive spreading or substantial flow along the tool surface

(Ref 6). This type of forging can be applied to sintered Al P/M compacts to enhance the metallurgical bonding across the interfaces where the oxide layer is broken (Ref 5).

The oxide layer thickness on Al powder produced by inert gas atomization (~ 3 nm) is thinner than that produced by air atomization (~ 7 nm), for a particle median diameter of 20 μm (Ref 7). Inert gas-atomized Al powders (with 4 nm oxide layer thickness) attain good particle bonding when sintered by spark plasma sintering (SPS), which disrupts the oxide layer (Ref 8). However, as the oxide layer thickness increases, it becomes harder to promote particle bonding during SPS due to the insufficient metal-to-metal contact (Ref 9). Rudinsky et al. (Ref 3) demonstrated that Alumix 431D consolidated by SPS suffers from poor sintering. Given that Alumix 431D powders contain air-atomized Al particles, it can be expected that the alumina layer present in air-atomized Al powders would be difficult to disrupt. Furthermore, the possible formation of a spinel layer arising from the reaction of Mg with the native alumina layer may require a higher applied load to break the oxide layer (Ref 9).

This study investigates the sintering behavior of a modified Alumix 431D alloy powder. The modification consisted of producing an Alumix 431D mixture using gas-atomized pure Al powders and the conventional master alloy. The modified Alumix 431D powder was consolidated using spark plasma sintering (SPS) and further forged by SPS upsetting. Bulk mechanical properties were evaluated through bending tests and fracture surface analysis.

2. Experimental Methods

To generate a modified Alumix 431D powder blend, the following procedure was applied. First, the original Alumix 431D powder from ECKA granules was sieved using a -325 mesh size to separate the air-atomized pure Al particles from the mixture. The sieved Alumix 431D powder, hereafter referred as the master alloy, presented an irregular and elongated morphology as depicted in Fig. 1(a). After sieving,

Mehmet Masum Tünçay, Department of Mining and Materials Engineering, McGill University, 3610 University Street, Montreal, QC H3A 0C5, Canada and Department of Metallurgical and Materials Engineering, Marmara University, 34722 Göztepe, Istanbul, Turkey; José Alberto Muñiz-Lerma and Mathieu Brochu, Department of Mining and Materials Engineering, McGill University, 3610 University Street, Montreal, QC H3A 0C5, Canada; and Donald Paul Bishop, Department of Mechanical Engineering, Dalhousie University, 1360 Barrington Street, Halifax, NS B3H 4R2, Canada. Contact e-mail: mathieu.brochu@mcgill.ca.

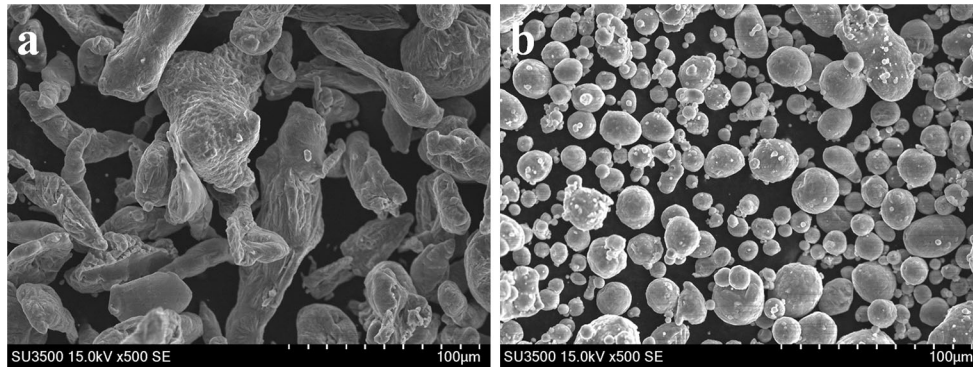


Fig. 1 Morphology of raw powders used to produce a modified Alumix 431D powder mixture, (a) master alloy and (b) gas-atomized Al (H15) powder

Table 1 Chemical compositions (wt.%) of the powders

ID	Powder	Al	Zn	Mg	Cu	Sn	Fe
A(a)	Alumix 431D	Bal.	5.6-6.4	2.4-3.0	1.5-2.0	0.1-0.3	...
B	Master alloy	Bal.	8.2	3.9	2.2	0.4	...
C(a)	Al (H15)	99.8	0.1
D	Modified Alumix 431D	Bal.	6.6	2.8	1.5	0.3	0.1

(a) Chemical composition provided by the supplier's certificate of analysis

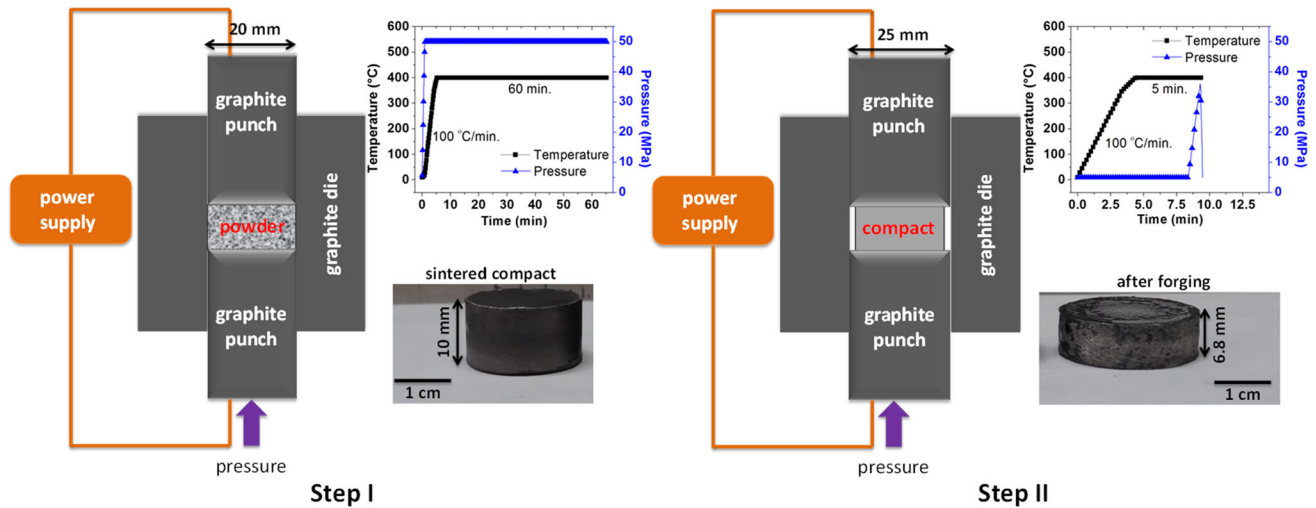


Fig. 2 Schematic of two-step SPS process

spherical gas-atomized Al (H15) powder (Fig. 1b), supplied by Valimet (Stockton, CA, USA), was mixed with the master alloy powder so that the final composition of the mixture was in the range of the original Alumix 431D. The powder mixing was carried out by placing the respective ratios of powders in a container, which was rotated at 50 rpm for 1 h. The chemical composition of the master alloy powder and the modified Alumix 431D was ascertained using inductively coupled plasma emission spectroscopy (ICP), and the results are given in Table 1.

The modified Alumix 431D powder was used for all experiments. A two-step process was applied to the powder using SPS: The first step was the sintering of the powder, and the second step was forging (see Fig. 2 for schematic). Six

cylindrical samples of 10 mm in height by 20 mm in diameter were sintered using an SPS 10-3 apparatus (Thermal Technologies Inc., Santa Rosa, CA, USA) equipped with a 20-mm-diameter graphite die-punch set (Isocar Graphite I-85, Electrodes Inc., Santa Fe Springs, CA). Sintering was performed at 400 °C under 50 MPa pressure and a vacuum of 6.6×10^{-2} torr for a 60-min holding time. Pressure was constant throughout the sintering cycle. An initial heating rate of 100 °C/min was used to reach 350 °C, after which the heating rate was slowed to 50 °C/min until 400 °C was reached in order to prevent overshooting of the target temperature. Temperature was measured using a C-type thermocouple placed in the bottom punch, which had a hole drilled to 2 mm from the surface of the sample. The forging step was carried out by

Table 2 Nomenclature and description of the samples processed

Nomenclature	Description
T1-D T6-D	As-sintered (1 h at 400 °C under 50 MPa, furnace cool) Heat treatment of T1-D sample (4 h at 450 °C, water quench, 24 h at 125 °C, air cool)
T1-D forged	Upset forging of T1-D sample (32% reduction in height at 400 °C after 4-min holding period, furnace cool)
T6-D forged	Heat treatment of T1-D forged sample (4 h at 450 °C, water quench, 24 h at 125 °C, air cool)

placing the 10-mm-tall sintered samples (three of them) in a 25-mm-diameter Isocarb Graphite I-85 die-punch set and heating them to 400 °C using the same heating rate procedure outlined above. Samples were kept at 400 °C for a period of 4 min and then deformed at that temperature with a maximum pressure of 36 MPa on the punch, using a loading rate of 0.55 MPa/s, taking 1 min to reach full pressure. The maximum compressive strain imposed on the samples was 32% due to the limitations in punch length. After forging, the samples were cooled to room temperature and removed from the SPS unit for analysis.

Bulk density was measured on sintered and forged samples using the Archimedeian method as described in ASTM standard B963-13 (Ref 10). To heat treat the produced samples, differential scanning calorimetry (DSC) was first conducted with a Netzsch STA 449F3 instrument to determine the initial melting temperature. For this purpose, 10 mg of the forged samples was heated up to 650 °C under flowing argon using a heating rate of 10 °C/min. An initial melting event with a peak temperature of 475 °C, which corresponds to the melting of the MgZn₂ phase (Ref 11), was observed. Therefore, a solutionizing temperature of 450 °C was used. T6 temper was applied to both sintered and forged samples using 4 h solutionizing at 450 °C, followed by artificial aging at 125 °C for 24 h after water quenching. The nomenclature and descriptions for all samples are presented in Table 2.

All samples were mounted, ground, and polished using 320, 400 grit papers and 9-, 3- μ m diamond suspensions with an end step of colloidal silica suspension on a Vibromet polisher. Microstructural analysis was performed with backscattered electron (BSE) imaging and energy-dispersive spectroscopy (EDS) using a Hitachi SU3500 SEM. X-ray diffraction (XRD) analysis was performed using a Bruker D8 Discovery x-ray diffractometer (Cu-source).

Mechanical properties were evaluated by microhardness and a three-point bending test. Microhardness was measured with a Clark Microhardness (CM-100AT) indenter using a load of 10 g; reported hardness values were the average of 10 indentations. Three-point bending tests (sample dimension 1.8 \times 4.3 \times 20 mm) were carried out using a Tinius Olsen H25K-S Instron with a crosshead travel speed of 10 mm/min and a support span of 18.75 mm. The flexural stress and strain values were obtained using the related equations which can be found elsewhere (Ref 12). Three tests were done on each sample. Fracture surface analysis was carried out using the same Hitachi SEM used for EDS.

3. Results and Discussion

3.1 Modified Alumix 431D Powder Characterization

The cross-section microstructure of the modified Alumix 431D powder used in this study is presented in Fig. 3. The low-

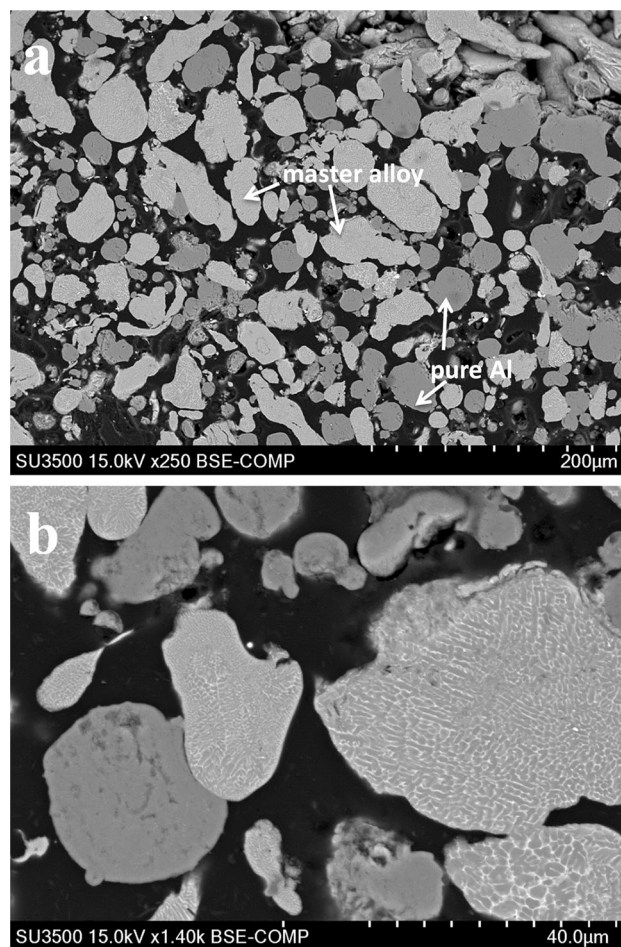


Fig. 3 Cross-section microstructures of the modified Alumix 431D at (a) low and (b) high magnification

magnification micrograph shown in Fig. 3(a) depicts the presence of irregular light gray particles from the master alloy powder in addition to spherical dark gray Al (H15) powders resulting from powder mixing. A high-magnification micrograph taken from the powder mixture and shown in Fig. 3(b) reveals the microstructure detail of the modified Alumix 431D powder. A fine cellular/dendritic microstructure characteristic of a rapid solidification processing is observed in the irregular master alloy particles with solute elements segregated in the interdendritic/cellular regions. The Al (H15) particles are present with no specific features in their microstructure aside from residual porosity resulting from the gas atomization process.

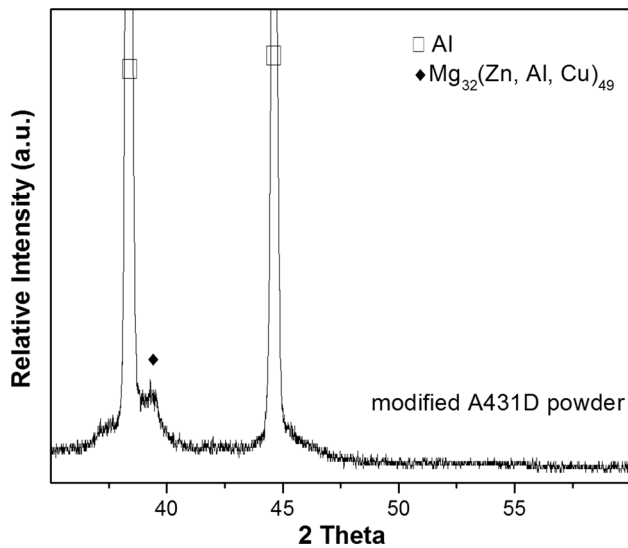


Fig. 4 XRD pattern of the modified Alumix 431D powder

The XRD pattern of the modified Alumix 431D powder is shown in Fig. 4. According to these findings, the white intermetallic compound present at the cell/dendrite boundaries of the master alloy particles corresponds to $\text{Mg}_{32}(\text{Zn}, \text{Al}, \text{Cu})_{49}$. The formation of this compound in rapidly solidified Al-Zn-Cu-Mg alloys has been also reported by Molnárová et al. (Ref 13), Taleghani et al. (Ref 14), and Becker et al. (Ref 15).

3.2 Spark Plasma Sintering of Modified Alumix 431D

SPS of the powder mixture (D) was carried out giving rise to a theoretical density (TD) of $98.7 \pm 0.1\%$, using 2.79 g/cm^3 as the full TD for the alloy (Ref 16). Representative BSE micrographs with corresponding EDS point analysis obtained after sintering are shown in Fig. 5(a)-(c). From the low-magnification BSE micrograph depicted in Fig. 5(a), a heterogeneous microstructure comprised of two distinct regions is observed. The first region, presented in Fig. 5(b), contains a large amount of bright secondary phases that correspond to remnants of the master alloy powders. EDS point analysis indicates that the secondary phases consist of Mg, Zn, Cu, and Al. The second region, shown in Fig. 5(c), has a low concentration of secondary phases. The low concentration of secondary phases found in the second region is due to the diffusion of solute elements from the master alloy particles into gas-atomized pure Al powders. A rudimentary calculation of the diffusion distance of the alloying elements in the master alloy after sintering is obtained by applying the analytic binary solution to the steady-state diffusion equation:

$$\frac{C_x - C_0}{C_s - C_0} = 1 - \operatorname{erf}\left(\frac{x}{2\sqrt{Dt}}\right), \quad (\text{Eq 1})$$

where C_s and C_0 are the concentrations of the diffusing species at each boundary, C_x is the concentration at distance x after a diffusion time t , and D is the interdiffusion coefficient. The diffusion coefficients of Zn, Mg, and Cu in Al are 1.8×10^{-15} , 6.6×10^{-15} , and $1.2 \times 10^{-14} \text{ m}^2/\text{s}$, respectively, at $400 \text{ }^\circ\text{C}$ [pre-exponential factor D_0 (m^2/s) and activation energy Q (kJ/mol) of Zn, Mg, and Cu in Al are, respectively, 1.19×10^{-5} and 116.1; 1.49×10^{-5} and 120.5; 4.44×10^{-5} and 133.9 (Ref 17)]. Using Eq 1, the diffusion distances of

Zn, Mg, and Cu in Al at $400 \text{ }^\circ\text{C}$ for 60 min are 29, 20, and $10 \text{ }\mu\text{m}$, respectively. Since the particle size distribution (D_{50}) of gas-atomized pure Al (H15) powder used in this study is $21 \text{ }\mu\text{m}$ (Ref 8), the solute atoms from surrounding Alumix 431D master alloy powder particles can diffuse into gas-atomized Al (H15). Hence, the formation of precipitates arising from the diffused elements during the SPS cooling step can occur.

The XRD pattern of the T1-D sample given in Fig. 7 indicates the presence of a MgZn_2 phase, as was also observed by LaDelpha et al. (Ref 16), Pieczonka et al. (Ref 18), and Rudinsky et al. (Ref 3). The formation of the MgZn_2 phase in the as-sintered samples can be attributed to the precipitation of diffused solute atoms during cooling and the transformation of the preexisting $\text{Mg}_{32}(\text{Zn}, \text{Al}, \text{Cu})_{49}$ phase in the master alloy particles during sintering. Molnárová et al. (Ref 13) report that $\text{Mg}_{32}(\text{Zn}, \text{Al}, \text{Cu})_{49}$, which is originally present in atomized Al-Zn-Mg-Cu alloy powder, is transformed into $\text{Mg}(\text{Zn}, \text{Cu}, \text{Al})_2$ during sintering. The formation of $\text{Mg}(\text{Zn}, \text{Al}, \text{Cu})_2$ precipitates from the initial $\text{Mg}_{32}(\text{Zn}, \text{Al}, \text{Cu})_{49}$ phase during sintering has been also reported by Taleghani et al. (Ref 14) and Becker et al. (Ref 15).

Following sintering, the T6 heat treatment was applied to the T1-D samples. Representative BSE micrographs of T6-D samples are shown in Fig. 5(d)-(f). A low-magnification micrograph presented in Fig. 5(d) indicates that full homogenization of the microstructure after T6 treatment was not obtained. Zones containing coarse precipitates and zones lacking coarse precipitates, as shown in Fig. 5(e) and (f), respectively, can still be distinguished within the microstructure. This observation indicates that the solutionizing treatment was not enough to completely dissolve the large secondary phases present in the microstructure. EDS point analysis reveals that most of the secondary phases present in the microstructure contain Mg, Zn, Cu, and Al. However, in isolated locations, such as the one indicated by the circular region pointed to by an arrow in Fig. 5(d) and magnified in Fig. 6, precipitates showing different BSE contrast due to compositional differences are observed. EDS point analysis of these precipitates indicates only the presence of Al, Cu, and Mg suggesting that an Al_2CuMg phase is also present in the microstructure. Mondolfo (Ref 19) reported that when the content of Cu in the alloy is larger than Mg, the formation of the Al_2CuMg phase can be promoted in the Al-Zn-Mg-Cu system. During the solutionizing treatment, $\text{Mg}(\text{Zn}, \text{Cu}, \text{Al})_2$ precipitates dissolve gradually into the α -Al matrix. During this process, the low diffusivity of Cu in α -Al compared to Mg and Zn can lead to localized regions with high Cu concentration. Hence, Al_2CuMg formation can be expected in these regions. Similarly, Fan et al. (Ref 20) reported formation of S phase (Al_2CuMg) during homogenization treatment of an Al-Zn-Mg-Cu alloy at $460 \text{ }^\circ\text{C}$ for 6 h.

The XRD pattern obtained from the T6-D sample (Fig. 7) shows that the matrix is mainly composed of α -Al and MgZn_2 phases. The intensity of the MgZn_2 peak is weaker than the as-sintered state, suggesting that this phase has been partly dissolved (Ref 20). The Al_2CuMg phase could not be detected by XRD as the volume fraction would be below the detection limit.

3.3 Spark Plasma Upsetting of Modified Alumix 431D

Upset forging by SPS was carried out on the sintered samples providing a 32% reduction in height. The final density

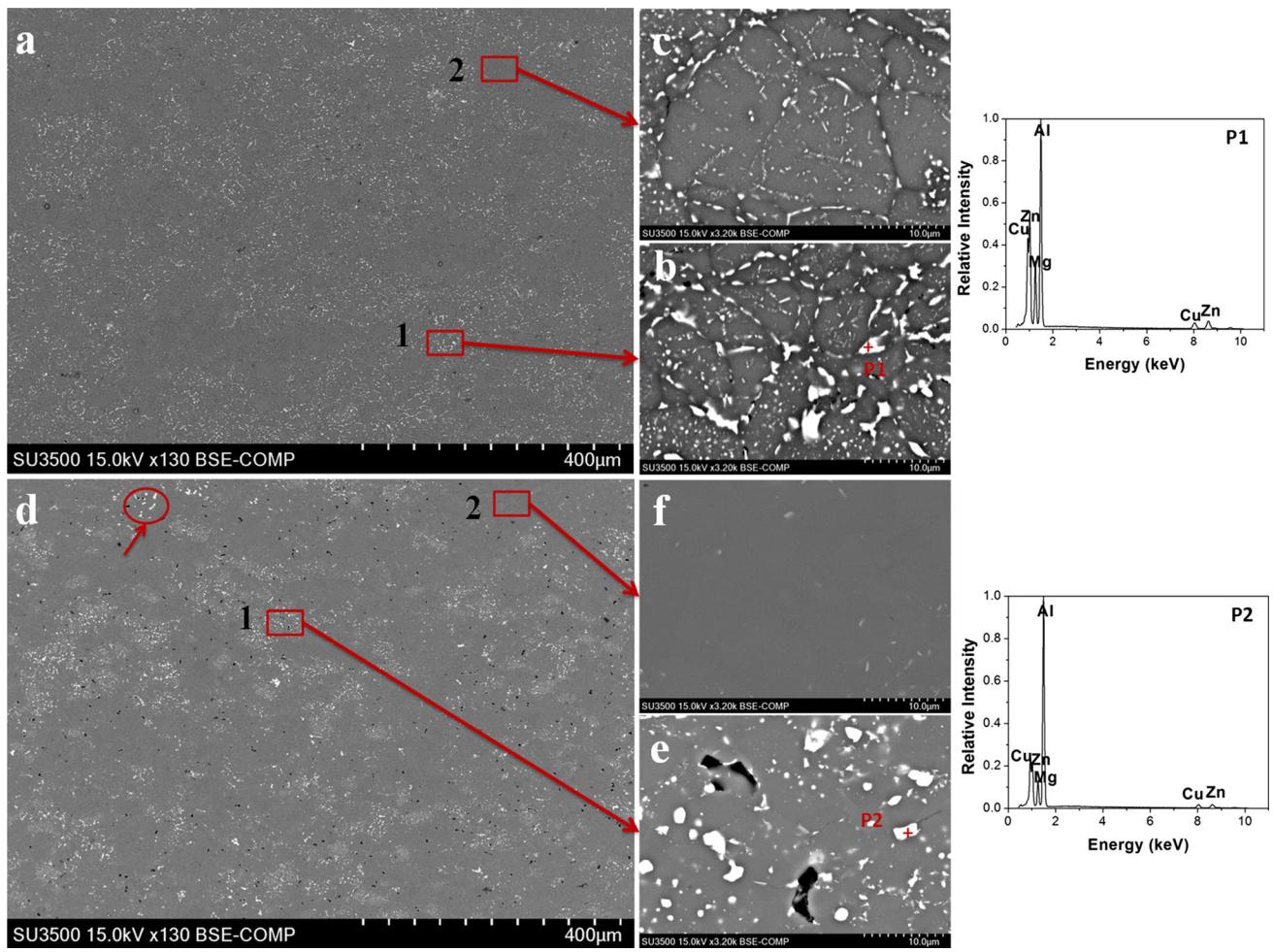


Fig. 5 Representative BSE micrographs of T1-D sample (a) low magnification, (b) high magnification for region 1, (c) high magnification for region 2, and T6-D sample (d) low magnification, (e) high magnification for region 1, (f) high magnification for region 2 with corresponding EDS point analysis

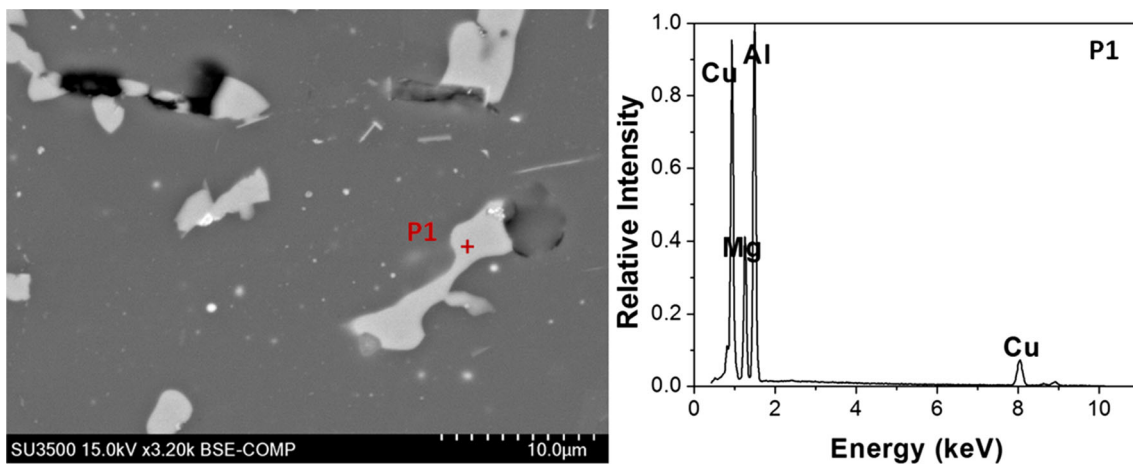


Fig. 6 High-magnification BSE micrograph of the circular region pointed to by arrow in Fig. 5(d) with corresponding EDS point analysis

attained after forging was $99.8 \pm 0.1\%$ TD. Characteristic BSE micrographs obtained from T1-D forged samples are presented in Fig. 8(a)-(c). The measured pore fraction using image analysis of Fig. 8a was 0.1%. Like the as-sintered samples, a heterogeneous microstructure consisting of the aforementioned

two regions persists. However, precipitation coarsening is observed in forged samples, best seen in the high-magnification BSE micrograph of the first region presented in Fig. 8(b). According to EDS point analysis, these precipitates exhibit Mg, Zn, Cu, and Al. Since the forged samples were heated to

400 °C, the precipitate coarsening occurs by the Ostwald ripening mechanism (Ref 21). Lang et al. (Ref 22) have reported a similar behavior for hot deformed AA 7050 alloy. Additionally, Deschamps et al. (Ref 23) state that warm

deformation accelerates the precipitation coarsening due to the formation of vacancies generated by plastic flow, enhancing solute diffusion. Similarly, Huo et al. (Ref 24) have shown that $MgZn_2$ precipitates present a linear coarsening behavior with increasing warm rolling reduction of AA7075. This coarsening behavior has been ascribed to accelerated coarsening kinetics due to plastic strain. Therefore, the application of forging can additionally contribute to the precipitation growth observed in this study.

T6 heat treatment was also carried out on the T1-D forged sample, and the corresponding BSE micrographs are presented in Fig. 8(d)-(f). The measured pore fraction using image analysis of Fig. 8d was 1.2%, which indicates increase in the porosity after the heat treatment. It is clear from Fig. 8(d) that the microstructure is not fully homogenized and has a similar appearance to the T6-D sample. Comparing the first region of T6-D forged sample (Fig. 8e) with the first region of T1-D forged sample (Fig. 8b) reveals that homogenization has partly occurred. On the other hand, full homogenization has been attained in the second region (Fig. 8f). EDS map analysis for a partly homogenized region of the T6-D forged sample is presented in Fig. 9. The EDS map reveals two distinct precipitates within the microstructure, one containing Al, Zn, Cu, and Mg associated with $Mg(Zn, Cu, Al)_2$ and a second precipitate containing Al, Cu, and Mg, possibly related to

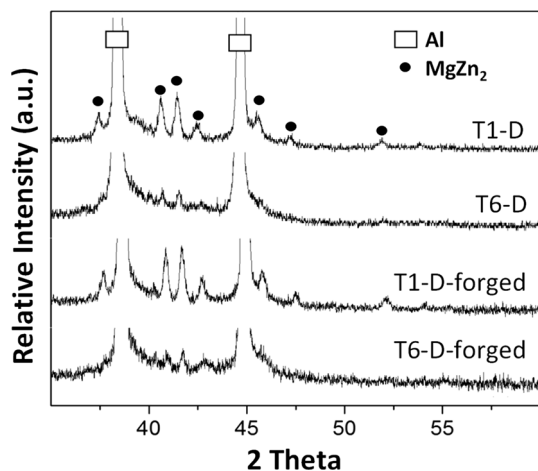


Fig. 7 XRD spectrum of T1-D, T6-D, T1-D forged, and T6-D forged samples

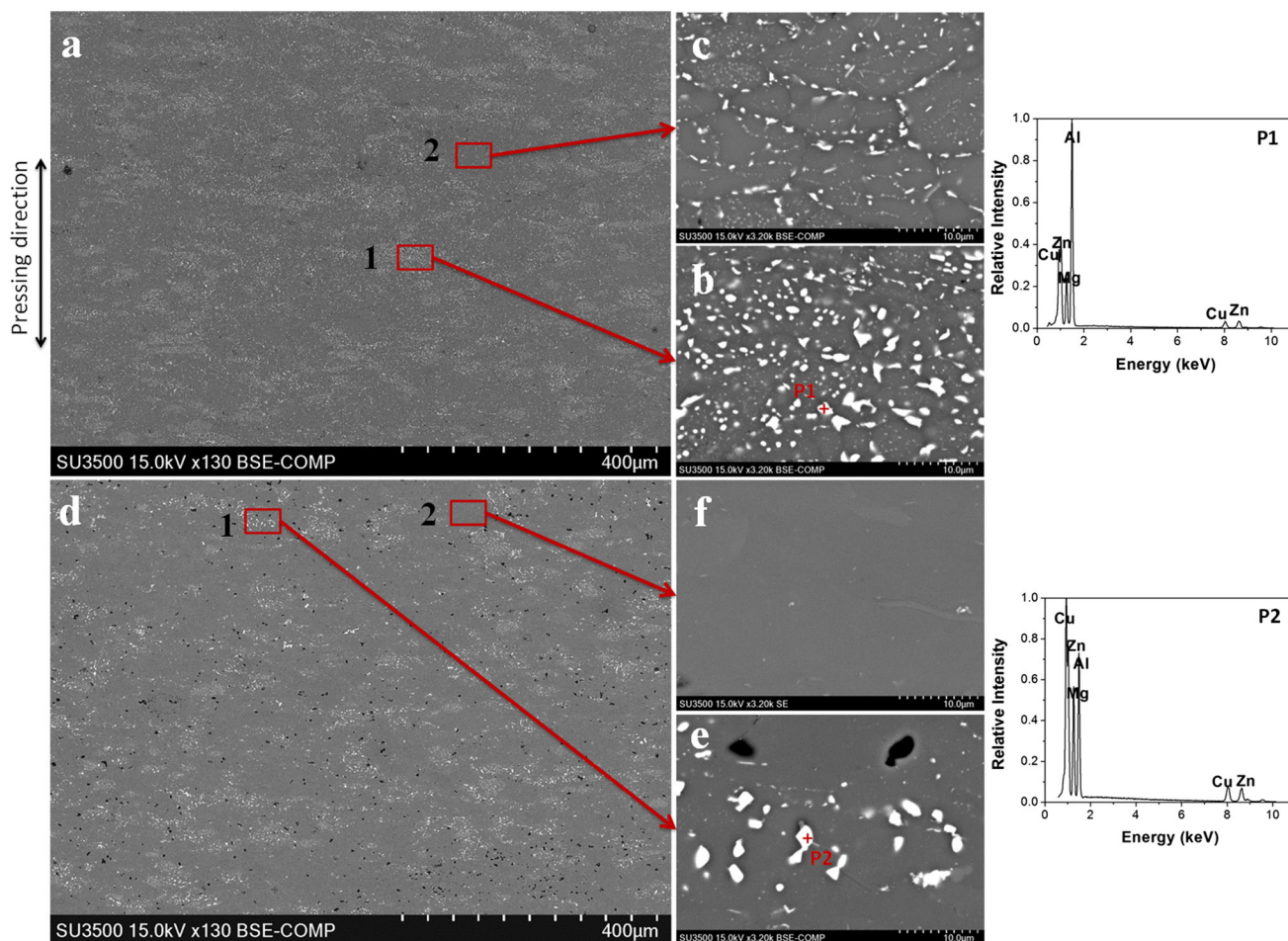


Fig. 8 Representative BSE micrographs of the T1-D forged sample (a) low magnification, (b) high magnification for region 1, (c) high magnification for region 2, and the T6-D forged sample (d) low magnification, (e) high magnification for region 1, (f) high magnification for region 2 with corresponding EDS point analysis

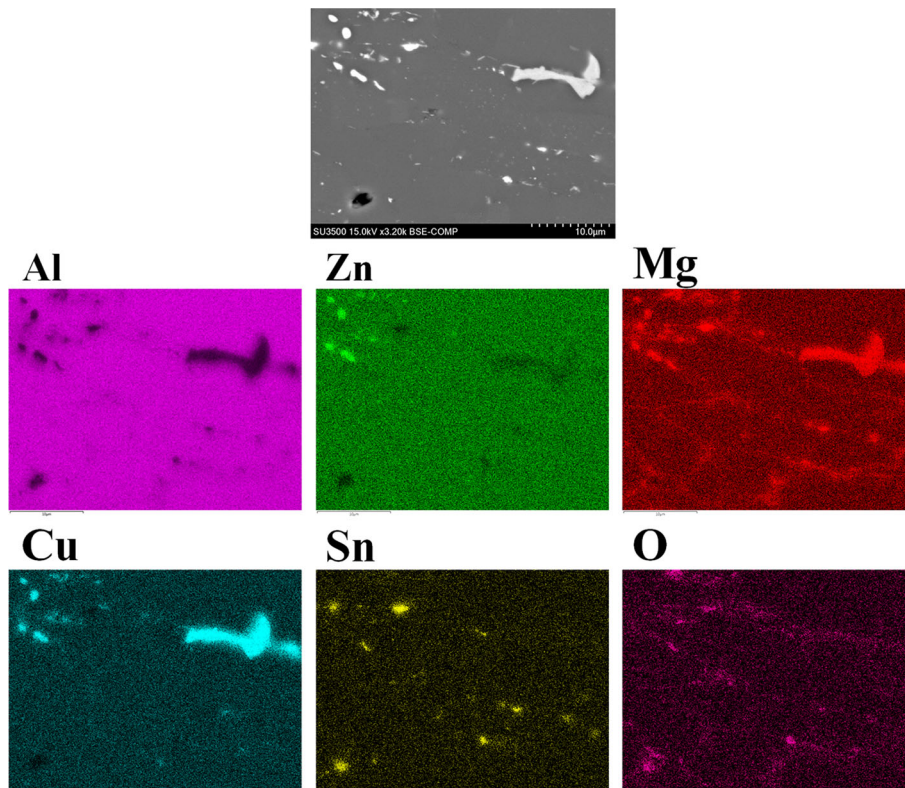


Fig. 9 A representative BSE micrograph (high magnification) and EDS maps of T6-D forged sample for the partly homogenized region

Table 3 Microhardness, given in Vickers hardness (HV), of samples

Samples	Region 1	Region 2	Average
T1-D (HV)	111 ± 2	119 ± 3	115 ± 3
T6-D (HV)	169 ± 3	177 ± 2	173 ± 2
T1-D forged (HV)	98 ± 1	107 ± 2	102 ± 2
T6-D forged (HV)	168 ± 3	177 ± 1	173 ± 3

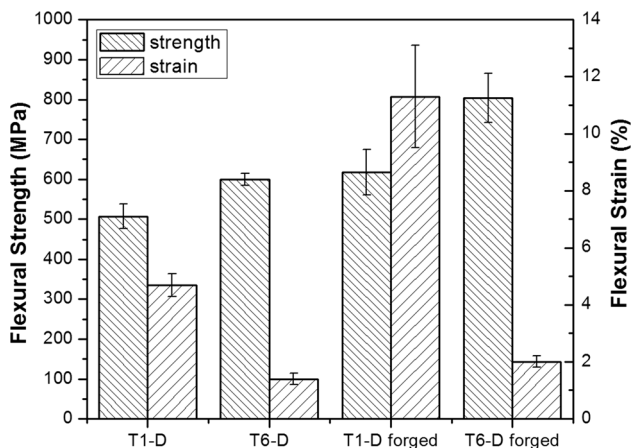


Fig. 10 Flexural properties of the samples from a three-point bending test

Al_2CuMg (S) phases. Clusters of Sn can be also recognized in the microstructure, consistent with the observations of Rudianto et al. (Ref 25) and Rudinsky et al. (Ref 3). Additionally, the

coexistence of O and Mg might be related to the formation of MgAl_2O_4 or MgO as a consequence of the reaction between Mg and Al_2O_3 layer on the powder particles (Ref 26), which was also observed by Rudianto et al. (Ref 25) for the sintering of Alumix 431D.

The XRD pattern presented in Fig. 7 confirms that MgZn_2 is still present in the T1-D forged sample and the T6-D forged sample. However, the relative intensity of the MgZn_2 phase decreased after T6 temper, suggesting that dissolution has partly occurred.

3.4 Mechanical Properties

As seen in Fig. 5 and 8, the overall microstructure of the T1-D, T6-D, T1-D forged, and T6-D forged samples consists of two distinct regions. Microhardness testing carried out on these samples, taking measurements in each region, provides the results presented in Table 3. The overall microhardness of each sample is reported as the average of the measurements from the two regions. In all samples, region 1 had lower hardness than region 2. For the T1-D sample, a decrease in hardness for the first region can be attributed to the larger size of precipitates since large particles with wide interparticle distance result in softening (Ref 27). For the T6-D sample, the lower hardness of region 1 can be attributed to incomplete homogenization. The microhardness of the second region, which was fully homogenized, corresponds to 177 ± 2 HV. This microhardness value is comparable with reported values; a hardness value of 87 HRB (180 HV) for SPS sintered AA7075 after T6 temper was reported by Chua et al. (Ref 28), equal to that of wrought T6 AA7075. LaDelpha et al. (Ref 16) obtained 86 HRB (176 HV) for T6 tempered Alumix 431D processed with liquid-phase sintering. The T1-D forged

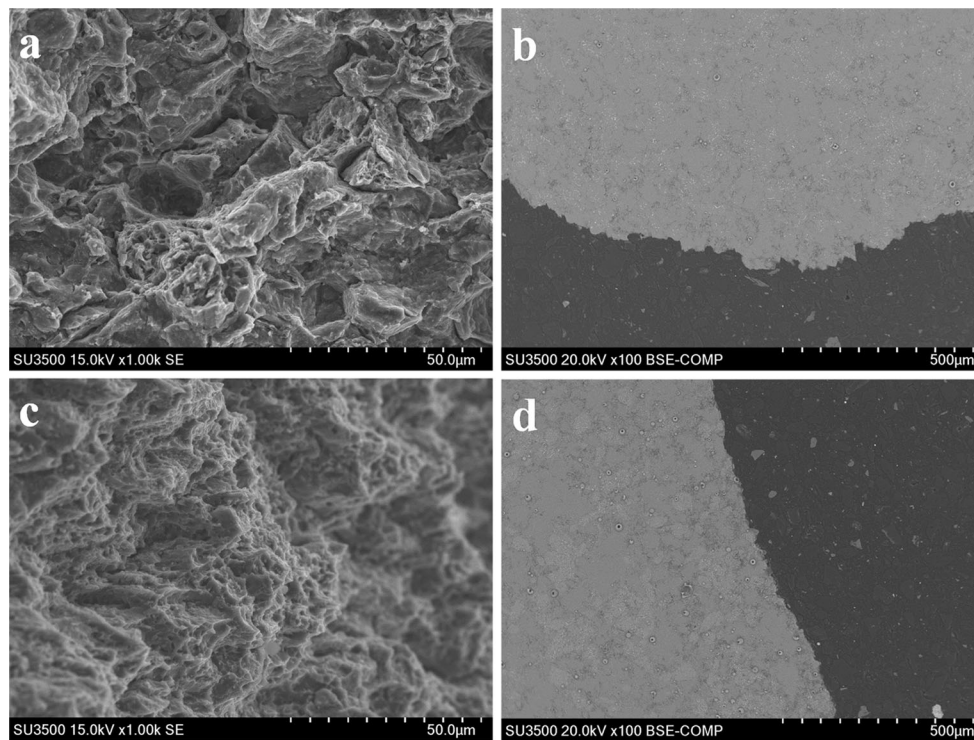


Fig. 11 Fracture (a) cross section of T1-D, (b) side view of T1-D, (c) cross section of T1-D forged and (d) side view of T1-D forged samples

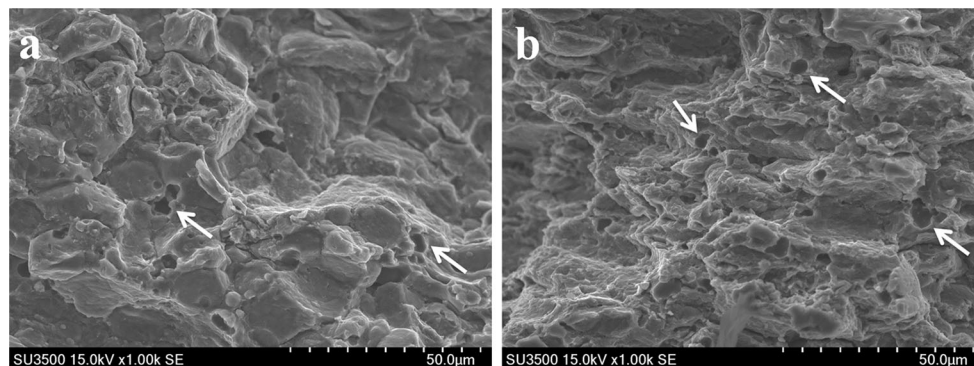


Fig. 12 Fracture (a) cross section of T6-D, (b) cross section of T6-D forged samples. Voids are indicated by arrows

sample had decreased hardness compared to the T1-D sample for both regions; this can be attributed to the growth of the precipitates after forging, as described in section 3.3. The T6-D forged sample had hardness values similar to the T6-D sample.

Three-point bending tests were carried out to evaluate flexural properties of the samples, and results are given in Fig. 10. Significant improvement in flexural properties is observed after forging as compared to the as-sintered state. Since the as-sintered samples were nearly fully dense, this improvement of the flexural properties after forging can be attributed not only to density but also to better particle bonding. Additionally, this gain in strength surpasses the potential loss in strength from growth of the precipitates as depicted in hardness measurements.

The fracture surface of the T1-D sample is presented in Fig. 11(a). When particle bonding occurs, the fracture surface shows the formation of dimples where the particle boundaries are not noticeable (Ref 29). The T1-D sample presents a brittle

fracture surface indicating prior particle boundaries, although few dimples can be seen. Additionally, the fracture side view (Fig. 11b) has bumps indicating that breakage occurred around the particles. A lack of bonding between particles has been also reported by Rudinsky et al. (Ref 3) for Alumix 431D sintered by SPS. Nevertheless, it was previously shown that SPS of gas-atomized Al (H15) provides good particle bonding where oxide layer disruption has mostly occurred in the as-sintered condition (Ref 8). In the current study, mixing of gas-atomized Al (H15) with the master alloy of Alumix 431D was performed in order to replace air-atomized pure Al. Since the pure Al in Alumix 431D blend was air-atomized powder and has thicker oxide layer than the gas-atomized powder (Ref 7) (and is thus harder to disrupt), it was expected that particle bonding could be obtained in the as-sintered condition with this mixture. However, the particle bonding problem could not be eliminated. Therefore, the lack of bonding between particles does not appear to be directly related solely to air-atomized Al powder in Alumix 431D.

The presence of Mg reduces Al_2O_3 as the free energy of formation of its oxide is more negative than that of aluminum oxide (Ref 30). However, a composite type of oxide layer can be formed requiring more force to disrupt (Ref 9). In Al-10 Mg alloy, Wakefield and Sharp (Ref 31) show that the surface oxide at room temperature is predominantly aluminum oxide with about 4 nm thickness and that the oxide film consists of both magnesium oxide and aluminum oxide with 8 nm thickness after it is subjected to 300 °C for 1 h. The surface of the oxide grown at 430 °C is almost completely magnesium oxide, giving a final thickness of 14 nm (Ref 31). Additionally, SPS of Al-Mg alloys was performed by Xie et al. (Ref 32) using 0.3, 1, 2.5, and 10 wt.% Mg, and this resulted in a high number of dimples in the fracture surface at low Mg content. According to their study, by increasing the amount of Mg the quantity of dimples is decreased and the thickness of the interface layer between particles is increased, yielding a brittle fracture with a lack of bonding between particles. Considering that Alumix 431D powder consists of master alloy particles and pure Al, the high amount of Mg content in the master alloy may lead to a thicker MgO or MgAl_2O_4 surface layer. Hence, the pressure used for the as-sintered state might not be sufficient to disrupt the oxide layer, but enhancement in the particle bonding can be obtained through forging, whereby rupture of the oxide films occurs under the application of greater strain coupled with appreciable amounts of lateral flow. In the T1-D forged sample, the fracture surface has more pronounced dimples and the particle boundaries are less detectable (Fig. 11c and d). Thus, the improvement in the flexural properties of the forged sample likely reflects better particle bonding and the incomplete bonding of Alumix 431D after SPS can be attributed to the formation of MgO/ MgAl_2O_4 (Ref 26) or a composite type of oxide layer produced during the process, rather than the air-atomized Al particles.

T6 temper was applied to the as-sintered and forged samples. An increase in strength and decrease in ductility are expected to occur following the age hardening heat treatment (Ref 33). Although this was observed in the current study, the significant loss in ductility following T6 treatment may also result from a lack of cohesion between particles that is intensified during the quenching step (Ref 3). However, as noted above, particle bonding was enhanced following the forging process. Accordingly, the ductility of the T6 tempered forged sample should be greater than in the T6 tempered sintered sample. In contrast to this expectation, the difference in ductility of the two samples was not significant. Therefore, deterioration of mechanical properties is most likely caused by a different mechanism. When the fracture surfaces of the T6-D and T6-D forged samples were investigated (Fig. 12), voids within the range of 1–6 μm were visible. From the micrographs of the T6 samples given in Fig. 5(e) and 8(e), pores within the same range can be observed. During the diffusion of a phase into a matrix, the dissolved phase can leave a void in the matrix (Ref 34). The voids observed after T6 temper may result from the dissolution of the second phases into the Al matrix. This explanation of the pore formation does not take into consideration the possible degassing of the powder, which may also explain the presence of the pores. However, more experimentation would have to be performed to fully discriminate the pore formation mechanism. The formation of these voids can be detrimental to the mechanical properties. Furthermore, the undissolved fraction of the secondary phases leads to embrittlement (Ref 11) and the presence of coarse particles ($> 1 \mu\text{m}$)

deteriorates toughness and fatigue performance (Ref 35). Therefore, in addition to the effect of the T6 temper on the flexural strain, the remaining secondary phases and the formation of voids during heat treatment negatively affect the flexural strain of the T6-D forged samples, even though particle bonding improves.

4. Conclusion

In this study, a master alloy of Alumix 431D powder was mixed with gas-atomized pure Al to obtain an Alumix 431D composition. Samples were sintered and forged by SPS and a T6 heat treatment applied. A final density above 98 and 99% theoretical density was obtained for as-sintered and forged samples, respectively. Flexural strength and strain of the as-sintered sample were improved after the forging process, which was mainly attributed to the enhancement of the particle bonding due to oxide layer disruption. A microhardness comparable to that of its wrought counterpart AA7075 was obtained after the T6 heat treatment. Significant loss in ductility following the T6 temper for both forged and as-sintered samples was observed, which may be mostly attributable to the formation of voids due to the dissolution of the secondary phases, the undissolved fraction of precipitates, and a lack of cohesion between particles.

Acknowledgments

The authors would like to acknowledge AUTO 21 (Grant no. C502-CPM) for their financial support and the Aluminum Research Centre—REGAL. The authors would like to thank The Council of Higher Education of Turkey and Marmara University for scholarships to Mr. Tünçay.

References

1. M. Omori, Sintering, Consolidation, Reaction and Crystal Growth by the Spark Plasma System (SPS), *Mater. Sci. Eng. A*, 2000, **287**, p 183–188
2. Z.A. Munir, Analytical Treatment of the Role of Surface Oxide Layers in the Sintering of Metals, *J. Mater. Sci.*, 1979, **14**, p 2733–2740
3. S. Rudinsky, P. Hendrickx, D.P. Bishop, and M. Brochu, Spark Plasma Sintering and Age Hardening of an Al-Zn-Mg Alloy Powder Blend, *Mater. Sci. Eng. A*, 2016, **650**, p 129–138
4. M.S. Mohammadi, A. Simchi, and C. Gierl, Phase Formation and Microstructural Evolution During Sintering of Al-Zn-Mg-Cu Alloys, *Powder Metall.*, 2010, **53**, p 62–70
5. T.C. Joshi, U. Prakash, and V.V. Dabhade, Microstructural Development During Hot Forging of Al 7075 Powder, *J. Alloys Compd.*, 2015, **639**, p 123–130
6. K. Lange, *Handbook of Metal Forming*, McGraw-Hill, New York, 1985
7. ASM Handbook, *Volume 07-Powder Metal Technologies and Applications*. (ASM International, 1998)
8. M.M. Tünçay, L. Nguyen, P. Hendrickx, and M. Brochu, Evaluation of the Particle Bonding for Aluminum Sample Produced by Spark Plasma Sintering, *J. Mater. Eng. Perform.*, 2016, **25**, p 4521–4528
9. P. Hendrickx, M.M. Tünçay, and M. Brochu, Recyclability Assessment of Al 7075 Chips Produced by Cold Comminution and Consolidation Using Spark Plasma Sintering, *Can. Metall. Q.*, 2016, **55**, p 94–103
10. ASTM B963-13, *Standard Test Methods for Oil Content, Oil-Impregnation Efficiency, and Interconnected Porosity of Sintered*

Powder Metallurgy (PM) Products Using Archimedes' Principle. (ASTM International, West Conshohocken, PA, 2013)

11. J.M. Martín, T. Gómez-Acebo, and F. Castro, Sintering Behaviour and Mechanical Properties of PM Al-Zn-Mg-Cu Alloy Containing Elemental Mg Additions, *Powder Metall.*, 2002, **45**, p 173–180
12. S. Rudinsky, J.M. Aguirre, G. Sweet, J. Milligan, D.P. Bishop, and M. Brochu, Spark Plasma Sintering of an Al-Based Powder Blend, *Mater. Sci. Eng. A*, 2015, **621**, p 18–27
13. O. Molnárová, P. Málek, F. Lukáč, and T. Chráska, Spark Plasma Sintering of a Gas Atomized Al 7075 Alloy: Microstructure and Properties, *Materials*, 2016, **9**, p 1004
14. M.A.J. Taleghani, E.M.R. Navas, and J.M. Torralba, Microstructural and Mechanical Characterisation of 7075 Aluminium Alloy Consolidated from a Premixed Powder by Cold Compaction and Hot Extrusion, *Mater. Des.*, 2014, **55**, p 674–682
15. H. Becker, M. Dopita, J. Stráská, P. Málek, M. Vilémová, and D. Rafaja, Microstructure and Properties of Spark Plasma Sintered Al-Zn-Mg-Cu Alloy, *Acta Phys Pol A*, 2015, **128**, p 602–605
16. A.D.P. LaDelpha, H. Neubing, and D.P. Bishop, Metallurgical Assessment of an Emerging Al-Zn-Mg-Cu P/M Alloy, *Mater. Sci. Eng. A*, 2009, **520**, p 105–113
17. Y. Du, Y.A. Chang, B. Huang, W. Gong, Z. Jin, H. Xu, Z. Yuan, Y. Liu, Y. He, and F.Y. Xie, Diffusion Coefficients of Some Solutes in fcc and Liquid Al: Critical Evaluation and Correlation, *Mater. Sci. Eng. A*, 2003, **363**, p 140–151
18. T. Pieczonka, J. Kazior, A. Szewczyk-Nykiel, M. Hebda, and M. Nykiel, Effect of Atmosphere on Sintering of Alumix 431D Powder, *Powder Metall.*, 2012, **55**, p 354–360
19. L.F. Mondolfo, *4-Aluminum-Zinc Alloys, Aluminum Alloys*, Butterworth-Heinemann, Oxford, 1976, p 842–882
20. X. Fan, D. Jiang, Q. Meng, and L. Zhong, The microstructural evolution of an Al-Zn-Mg-Cu Alloy During Homogenization, *Mater. Lett.*, 2006, **60**, p 1475–1479
21. R.E. Smallman and A.H.W. Ngan, *Physical Metallurgy and Advanced Materials*, 7th ed., Elsevier, Amsterdam, 2007
22. Y. Lang, Y. Cai, H. Cui, and J. Zhang, Effect of Strain-Induced Precipitation on the Low Angle Grain Boundary in AA7050 Aluminum Alloy, *Mater. Des.*, 2011, **32**, p 4241–4246
23. A. Deschamps, G. Fribourg, Y. Bréchet, J.L. Chemin, and C.R. Hutchinson, In Situ Evaluation of Dynamic Precipitation During Plastic Straining of an Al-Zn-Mg-Cu Alloy, *Acta Mater.*, 2012, **60**, p 1905–1916
24. W.T. Huo, J.T. Shi, L.G. Hou, and J.S. Zhang, An Improved Thermo-Mechanical Treatment of High-Strength Al-Zn-Mg-Cu Alloy for Effective Grain Refinement and Ductility Modification, *J. Mater. Process. Technol.*, 2017, **239**, p 303–314
25. H. Rudianto, G.J. Jang, S.S. Yang, Y.J. Kim, and I. Dlouhy, Evaluation of Sintering Behavior of Premix Al-Zn-Mg-Cu Alloy Powder, *Adv. Mater. Sci. Eng.*, 2015, **2015**, p 8
26. G. Xie, O. Ohashi, M. Song, K. Mitsuishi, and K. Furuya, Reduction Mechanism of Surface Oxide Films and Characterization of Formations on Pulse Electric-Current Sintered Al-Mg alloy Powders, *Appl. Surf. Sci.*, 2005, **241**, p 102–106
27. R.E. Reed-Hill and R. Abbaschian, *Physical Metallurgy Principles*, PWS Pub. Co., Boston, 1994
28. A.S. Chua, M. Brochu, and D.P. Bishop, Spark Plasma Sintering of Prealloyed Aluminium Powders, *Powder Metall.*, 2015, **58**, p 51–60
29. M. Zadra, F. Casari, L. Girardini, and A. Molinari, Spark Plasma Sintering of Pure Aluminium Powder: Mechanical Properties and Fracture Analysis, *Powder Metall.*, 2007, **50**, p 40–45
30. R.N. Lumley, T.B. Sercombe, and G.M. Schaffer, Surface Oxide and the Role of Magnesium During the Sintering of Aluminum, *Metall. Mater. Trans. A*, 1999, **30**, p 457–463
31. G.R. Wakefield and R.M. Sharp, The Composition of Oxides Formed on Al-Mg Alloys, *Appl. Surf. Sci.*, 1991, **51**, p 95–102
32. G. Xie, O. Ohashi, T. Sato, N. Yamaguchi, M. Song, K. Mitsuishi, and K. Furuya, Effect of Mg on the Sintering of Al-Mg Alloy Powders by Pulse Electric-Current Sintering Process, *Mater. Trans.*, 2004, **45**, p 904–909
33. A.D. Isadare, B. Aremo, M.O. Adeoye, O.J. Olawale, and M.D. Shittu, Effect of Heat Treatment on Some Mechanical Properties of 7075 Aluminium Alloy, *Mater. Res.*, 2013, **16**, p 190–194
34. M. Brochu, B. Gauntt, T. Zimmerly, A. Ayala, and R. Loehman, Fabrication of UHTCs by Conversion of Dynamically Consolidated Zr⁺ B and Hf⁺ B Powder Mixtures, *J. Am. Ceram. Soc.*, 2008, **91**, p 2815–2822
35. X.-G. Fan, D.-M. Jiang, Q.-C. Meng, B.-Y. Zhang, and T. Wang, Evolution of Eutectic Structures in Al-Zn-Mg-Cu Alloys During Heat Treatment, *Trans. Nonferrous Met. Soc. China*, 2006, **16**, p 577–581